ORIGINAL ARTICLE

Operational performance and metal droplet formation in pulsed-shielded metal arc underwater welding

Andrés M. Moreno-Uribe[1,2] · Leandro Vaccari[1] · Alexandre Q. Bracarense[2] · Hans J. Maier[1] · Thomas Hassel[1]

Abstract

Underwater Shielded Metal Arc Welding (SMAW) is highly affected by the welding depth. The arc and molten metal in contact with the surrounding environment cause operational and metallurgical challenges regarding arc stability, metal transfer, gas formation, high-cooling rates, and diffusible hydrogen uptake. The hydrostatic pressure causes losses in consumable fusion efficiency, constricts the arc, increases the number of short-circuit events, and consequently decreases the welded joint's process quality. In the present study, the novel approach of pulsed welding current is applied to wet shielded metal arc welding and is operational characteristics are evaluated in detail. Automated welding using an arc-voltage control system was used to obtain reproducible results. For the pulse conditions, two values of pulse current combinations, taking 140 A as the mean value, were set (ΔI of 40 A and 80 A). The same pulse and base duration were chosen, giving pulsing frequencies of 2.5 Hz and 25 Hz. The voltage and current signals were acquired and the short-circuit numbers and melting rates were calculated by processing the data stability factors. As a result, it was possible to weld with lower average welding currents through pulsed-current technology. This new approach can improve the stability of the wet SMAW process and contribute to obtaining better-quality welds without any changes for the underwater welder.

Keywords Pulsed welding · Covered electrode · Welding metallurgy · Metal transfer · Underwater welding · Process stability

1 Introduction

Due to the low implementation cost and acceptable performance [1, 2], the wet shielded metal arc welding (SMAW) process is the most applied technique in underwater welding [3]. However, problems inherent to the depth-related pressure conditions [4] and the surrounding environment [5] affect the structural integrity of welded joints [6]. One of the main challenges is the instability caused by hydrostatic pressure, which affects the operational performance of the process. This in turn has a key influence on the final quality of the weld metal deposited [7]. For instance, the

voltage–current range within which acceptable wet welds can be produced decreases with increasing depth [8]. The general trend among subsea technicians and commercial divers to counteract the constriction of the electric arc generated by the depth of operation is to increase the welding current. However, an increase in the diffusible hydrogen content contained in the weld results from an increase in the welding current, as stated by Fydrych et al. [9]. Furthermore, the welding current defines characteristics such as the welded joint's fusion depth, the consumable deposition rate, and the metal transfer mode [10].

Metal transfer plays a crucial role in welding [11]. The elements that make up the coating of the welding electrodes actively influence the characteristics of the arc and the composition and chemical properties of the liquid metal and the slag. In fact, the phenomenon of metal transfer with covered electrodes is more complex, as stated by Modenesi and Uribe [12].

Liquid weld metal and the metal droplet at the tip of the electrode interact with the surrounding environment during welding [13]. Regarding mass transfer, as the metal droplet

✉ Andrés M. Moreno-Uribe
   uribe@iw.uni-hannover.de

1 Institut für Werkstoffkunde (Materials Science), Leibniz Universität Hannover, An der Universität 2, 30823 Garbsen, Germany

2 Federal University of Minas Gerais, Graduate Program in Mechanical Engineering, Pres. Antônio Carlos Av. 6627, Belo Horizonte 31270-901, Brazil
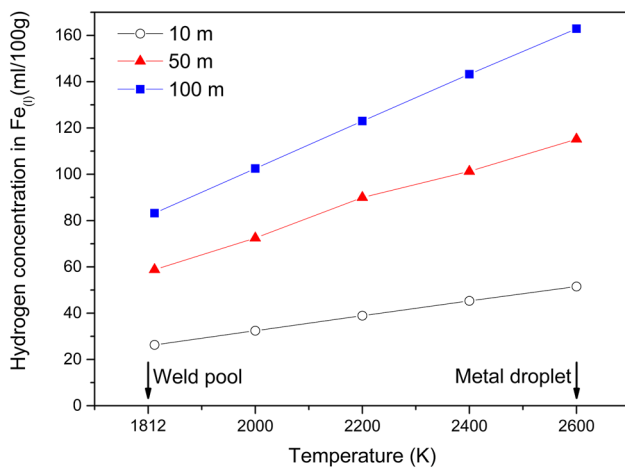
Fig. 1 H content in $Fe_{(l)}$ as a function of temperature and water depth; plot based on data generated through thermochemical calculations on the water molecule process decomposition; recompiled from Quintana Puchol et al. [16, 17]

travels through the plasma column and into the weld pool, it undergoes a complicated thermal cycle that promotes intense interaction between the contact phases [14]. In this way, the higher temperatures and the greater specific area of interaction, if compared to the weld pool, make the metal droplet an auspicious place for the penetration of gases [15]. Figure 1 reports higher hydrogen concentrations at 2600 K, a temperature corresponding to those of droplets of the filler metal located on the electrode tip and the arc (once the droplet flows freely through the arc column), as stated by Quintana Puchol et al. [16, 17]. On the other hand, the authors relate the lowest temperatures to the region of the weld pool (Fig. 1), where gas-absorption reactions occur but in a less intense way. As reported by Deyev and Deyev [18], the primary stage at which the reactions between the molten metal and the gas atmosphere occurs is during the drop phase.

Regarding underwater wet welding, Quintana Puchol et al. [16] mentioned that hydrogen and oxygen, which are the fundamental products of the decomposition of the water molecule, interact intensely with the metal droplet and the weld pool, causing pores, cracks, and non-metallic inclusions. Thus, it is essential to understand and control their absorption due to the gases dissolved in the liquid weld metal that can cause different negative effects on the welded joint.

Experimental data from several authors suggest that a gas bubble expands inside a metal droplet during its growth at the electrode tip, detachment, and transfer in the electric arc. For example, Larson [19] proposed one of the first mechanisms in which chemical reactions generate and expand a gas bubble inside the metal droplet. Brandi et al. [20] and Perez and Liu [21] found strong evidence that the gas bubble generation inside the metal droplets from

covered electrodes happens in welds made under onshore and offshore conditions. Observations made by Pessoa [22] suggested that the amount of gas transported inside the droplets depends on the time of formation and transfer in the arc. Also, particle size analysis showed that smaller droplets with lower internal porosity are produced at higher current values, as Perez and Liu [21] mentioned. For his part, Turani [23] observed that droplets with a larger diameter contain greater porosity. Considering the above, Deyev and Deyev [18] noted that decreasing the size of the electrode metal droplet could lead to a decrease in the levels of N, H, and O in the weld metal. Hence Xu et al. [24] suggested that underwater welding studies should focus on controlling and reducing gas in metal droplets.

At this point, one can infer that the control of the characteristics of the metal droplet (e.g., particle size) and its interaction time with the surrounding environment (e.g., metal transfer mode and detachment frequency) are essential for defining the final weld metal composition. However, according to Jia et al. [25], obtaining high-frequency droplet transfer with small-diameter droplets is challenging. On the other hand, favorable characteristics in the detachment frequency of the metal droplets or influencing the current signal aiming to modify the size of the metal droplet could be reached through the control of the metal transfer. This could be achieved through pulsed-current metal transfer, initially developed for MIG welding. In addition, applying pulsed current to covered electrodes could help overcome limitations inherent to the underwater wet SMAW process, such as an electric arc requiring a higher energy supply than in atmospheric conditions to overcome the instability barrier imposed by the depth and the aqueous environment.

Accordingly, the present study aimed at evaluating the operational performance of the pulsed current in the covered electrode wet SMAW process, and to analyze the influence of the process parameters on the final chemical composition of the weld metal, considering phenomena related to metal transfer and melting rate underwater. In addition, this exploratory study is expected to serve as a basis for optimization of the wide range of parameters possible with this control method.

2 Methodology

2.1 Equipment

All the experiments were carried out in a fresh water basin. An automated two-axes system for underwater welding was used to set a constant speed during the welding trials. In addition, an AVC (Automated Voltage Control) was used to balance the feed rate and target voltage.

Two power sources were used in the experiments. For the constant current welds (CC), the power source *400 E-UW* (*AMT GmbH; Germany)* was used. This DC welding machine operates with a current between 20 and 400 A and a maximum open-circuit voltage of 60 V. For the pulsed-current welds, the power source *Tetrix 1002 DC synergic* (*EWM AG; Germany)* was employed. The pulse TIG (Tungsten Inert Gas) operation function was chosen to weld in pulsed-current mode with a covered electrode. In addition, the software *PC 300XQ (EWM AG; Germany)* was used to configure the welding parameters, such as the open-circuit voltage (60 V), the peak current, base current, and frequency.

Figure 2 compares the voltage–current diagrams during the constant current welding process at 140 A to examine the differences between both power supply machines used. The dynamic characteristics of the *Tetrix 1002 DC synergic* power supply in SMAW operation mode exhibited a more concentrated distribution and smaller short-circuit cloud (Fig. 2—blue ellipse), resulting in a more stable behavior as compared to the AMT welding machine. Although the dynamic response of the power source generates differences in arc behavior and stability [26], for the purposes of this research, the implications of the dynamic performance of the welding power source were not examined.

The acquisition of the welding current and arc-voltage signals of the electric arc was possible through the use of a *3SR PO* system (*IMC Soldagem; Brazil)*. The data acquisition rate was 5 kHz.

2.2 Experimental design and materials

Table 1 shows the experimental parameters and their values as used in the present study. The basic idea was to compare constant and pulsed current. This was achieved by
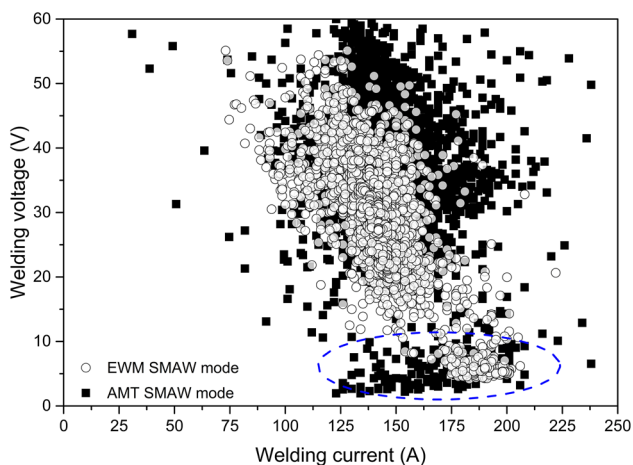

Fig. 2 Voltage–current diagram for power supply comparison during bead-on-plate CC welds at 140 A in shallow water

Table 1 Welding parameters used in the design of the experiments

Factor	Level	
	Low	High
Pulse frequency (Hz)*	2.5	25
ΔI** (A)	80	40
I_m (A)	120	140

*Note that Scotti and Ponomarev [27] recommend operating with pulse frequencies greater than 30 Hz to avoid epileptic reactions of the welder or increased eye fatigue. **See the chart provided in Fig. 3

conducting experiments with a CC power source working at 140 A and in addition using a welding machine that supplied pulsed current operating at a mean welding current (I_m) of = 140 A. In addition, two mean welding current levels were compared with the pulsed-current condition: 120 A vs 140 A. Thus, for all the experiments, two frequencies levels and two values of peak-base current combinations (ΔI) were defined. In this way, for example, taking 140 A as the mean welding current value, $\Delta I = 80$ A represents a peak current of 180 A and 100 A as the base current. Table 2 shows the parameters that were kept constant throughout the investigation. Three replicates were made for each condition of the experiment.

Figure 3 shows the range of parameters studied in the experiments. For reference, the operating range of the welding current for the AQUAWELD electrode, as recommended by the manufacturer [28], is marked by the orange dash-dotted lines. The red-dashed line represents the target voltage for all experiments (AVC setpoint). The grey area marks the region for which the AVC system was designed. The green area shows the experiments' application area. It can be compared with the yellow point, which identifies the operating welding current value used. The white point on the green band represents a no-operation point, at which it is impracticable to work with a 3.25 mm AQUAWELD electrode with a constant current source when using an AVC system.

2.3 Experimental data

The results of the experiments were separated into four groups: responses related to arc physics, metal transfer characterization, weld bead geometry, and weld pool chemistry. Fisher's least significant difference (LSD) was the mean comparison method used to plot the results, considering *p* values significance level through asterisks symbol with a bracket. The assumption of normal distribution was checked
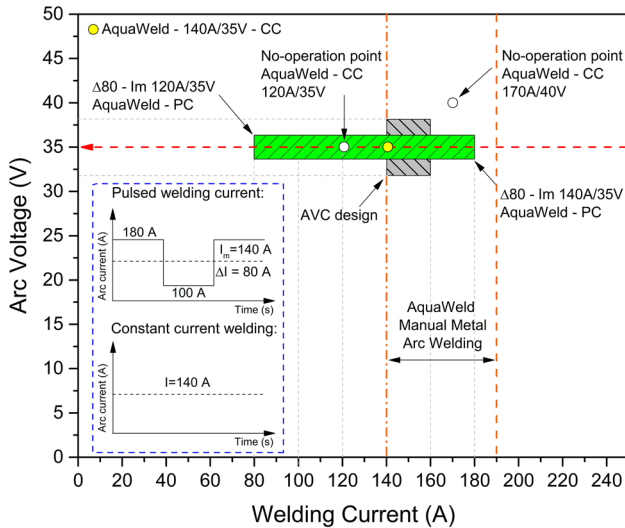
Fig. 3 Welding current and arc-voltage chart showing the parameter area covered in the experiments; the schematic diagram within the blue dashed-line box illustrates oscillograms for constant current operation mode and one of the pulsed-current configurations used in this study; I nominal welding current, I_m mean welding current, CC constant current, PC pulsed current

Table 2 Parameters kept constant in the welding experiments

Polarity	DCEN
Base metal	S355J2
Electrode	Rutile-basic-covered electrode E 38 0 Z RB 2 UW 20 fr (DIN 2302)—AQUAWELD [28]
Depth	0.5 m
Duty load cycle	50%
AVC target voltage	35 V
Welding speed	0.2 mm/s (1.2 cm/min)
Nominal electrode diameter	3.25 mm
Welding position	PA (ISO 6947)
Electrode configuration	90° to the base metal

for all statistical procedures. To verify the assumption of normal distribution, the Anderson–Darling and Bartlett tests were applied, as specified by Montgomery and Runger [29].

2.3.1 Arc analysis

The melting rate was calculated as a consumption ratio for the covered electrodes, i.e., the melting rate is the difference between the electrode's initial length and the electrode's remaining length after melting, divided by the total welding time [30]. In addition, the electrode feed rate was calculated for 20 s of the total welding time. For this, the movement of the welding system's Z-axis (i.e., the movement of the

electrode) was measured. Then, the first derivative of the position vector with respect to time was computed, and thus the feed rate was obtained. Figure 4 shows the displacement profile of the electrode compared to the voltage during the welding process. Furthermore, a first and second feed rate was established for 10 s at the beginning and end of the process. The first and second feed rates were used to evaluate possible operational changes between the beginning and the end of the welding process. Pistorius and Liu [31] noted significant changes in the number of short-circuit events and the size of transferred metal droplets while consuming basic, rutile, and cellulosic slag systems electrodes. Also, changes in the weld metal composition along the weld bead were reported by Bracarense and Liu [32]. Recently, Liberato et al. [33] noticed in measurements of the electrical resistance during short-circuit periods that as the electrode is consumed, the electrical resistance tends to drop, which could alter the melting rate.

To evaluate the system's response to the welding parameters and define a process stability index, the coefficient of variation of the manipulated variable was calculated. The manipulated variable was formed from the sum of the three elements of the PID controller (AVC programming and control logic). The P, I, and D terms were kept constant during all the experiments. Figure 5 shows the record of the manipulated variable, the arc voltage, and the target voltage during a pulsed-current welding process. In the present study, when quantitatively expressing the average value of the manipulated variable and its standard deviation, it becomes unfeasible to compare the pulsed and constant current conditions as a consequence of the high variance of the output signal. For that reason, it is more helpful to measure the distribution in relative terms through the proportion between the standard deviation and the mean manipulated variable value, i.e., the
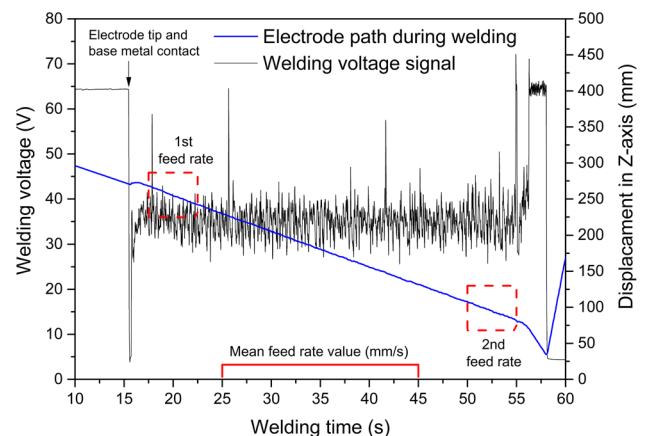

Fig. 4 Methodology for the feed rate definition: The red dashed-line boxes display the calculation base of the first and second feed rates
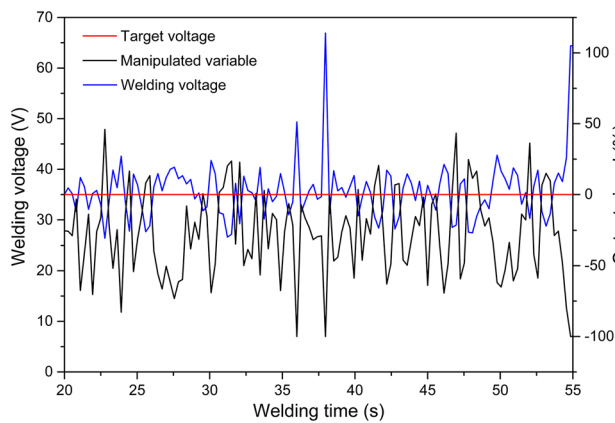
Fig. 5 Target voltage, arc voltage, and manipulated variable as recorded in the PID controlled setup

Fig. 6 Dynamic threshold value definition; 3.25 mm rutile-based electrode welded in 0.5 m and 60 m operating depth, using a gravity welding device at 120 A—straight polarity

coefficient of variation, as stated by Scotti and Ponomarev [27].

The average welding current was calculated from the quasi-stable region of the welding current oscillogram for 20 s. Also, the Root Mean Square (I_{RMS}) value of the current was calculated based on the formulation described in the work of Ghosh [34]. Likewise, the number of short circuits was calculated through the *Sinal software* routine [35] applied to the arc-voltage oscillogram. Based on the work developed by Amaral et al. [36], the number of times the voltage signal reached a given threshold value was calculated. This way, the number of short circuits occurring in 20 s was obtained. In addition, the arc voltage during open arc periods (OAV) was calculated during the same time (voltage data between the dynamic threshold value and 50 V).

Regarding the dynamic threshold value, factors such as polarity or operating hydrostatic pressure influence the power balance in the electric arc regions, affecting the performance of the process [37]. As seen in Fig. 6, under the effect of higher water depth, the arc-voltage distribution shifts to lower values. Thus, if the black arrow mark is considered a threshold value in the characterization of the arc regions, there would be a loss of data for the voltage distribution referring to 60 m depth. On the other hand, the blue arrow mark indicates the best spot to divide the bimodal distribution, referring to the 60 m data points.

2.3.1.1 Particle size analysis The transferred metal droplets were collected and analyzed to compare the constant and pulsed-current operating modes and the effect of pulse frequency on metal transfer with the covered electrode. Based on the work carried out by Moreno-Uribe et al. [38], a droplet collector device was implemented. Figure 7 shows a copper plate inclined to the collector container. The high-electrical conductivity of copper facilitated the ignition of
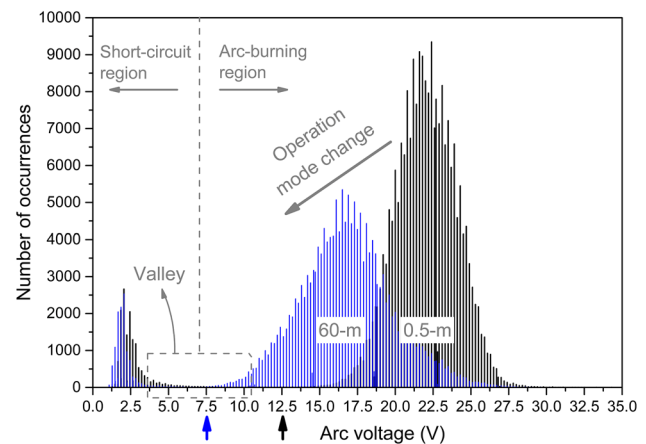
the arc, and its hig- thermal conductivity prevented the generation of a weld pool on the copper surface when the whole system was immersed in water. Thus, the droplets fell into a container, and could be collected for analysis.

The tests were conducted only for three experimental conditions: 140 A at constant current using a constant current welding machine and the pulsed-current power source with a mean welding current of 140 A, ΔI40, and 2.5 Hz and 25 Hz pulse frequencies. For each experimental condition, four electrodes were used. This process was replicated three times.

For granulometric classification, sieves according to ASTM E11-22 were employed (2.8 mm, 2.0 mm, 1.4 mm, 1.0 mm, 710 μm, and 510 μm), following the range of sieve openings recommended by Turani [23]. The remaining slag particles, after magnetic separation, were segregated from the metal droplets using a Retsch vibratory sieve shaker. Weighing the material retained in each mesh and passing through mesh 510 μm was performed using a *Mettler Toledo* analytical balance model *PH204S* with a maximum capacity of 220 g and an accuracy of 0.1 mg.

The droplets were counted using a particle size analysis method through a computer vision algorithm developed in *Python* to apply binarization, segmentation, and contour identification. In addition, samples from the granulometric classification were embedded with resin and ground until reaching the characteristic mesh opening diameter of the cross-section such that it was possible to verify the presence of voids inside.

A high-speed camera *Photron FASTCAM SA5* (5000-fps) was used to capture the metal transfer from the covered electrode. The system was equipped with a *Nikon SIGMA* 180 mm 1:3.5 F/22 aperture and an 810 ± 10 nm bandpass filter. A *Cavitar* laser illumination was used to visualize the
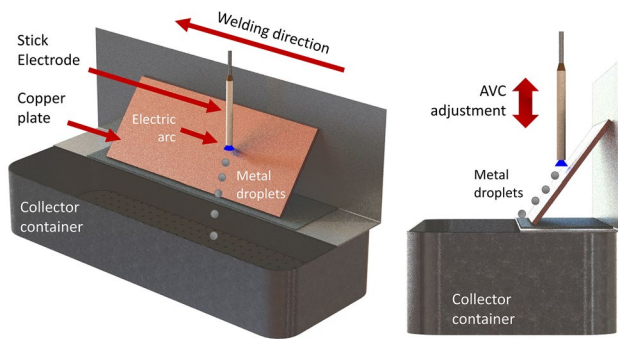
Fig. 7 Schematic showing the device used to collect the metal droplets

Fig. 8 Coefficient of variation (CV) plot of the manipulated variable for constant current and pulsed current at 140 A (mean current = nominal current): (**a**) and comparison between mean welding current levels: 120 A vs 140 A (**b**); *$p \le 0.05$, **$p \le 0.01$, ***$p \le 0.001$

metal transfer process. Due to bubbles and welding fumes typically affecting high-speed recording techniques [25], the videos were acquired under the onshore conditions. In that way, the image acquisition in the welding process focused on analyzing the detachment of metal droplets due to constant and pulsed-current welding conditions, leaving aside the interaction of the metal droplets with the welding pool or the water.

2.3.1.2 Weld bead geometry analysis Fourteen cm of bead-on-plate were welded for each combination of the different welding parameters. Samples of 10 mm length, taken from the center of each weld bead, were then metallographically analyzed. The software *ImageJ* was used to measure the depth of fusion (penetration in mm).

2.3.1.3 Welding chemistry analysis Six samples of geometry C were welded according to ISO 3690:2018, an industrial standard adjusted for underwater wet welding to estimate the diffusible hydrogen content in the weld metal (mL/100 g), following the methodology of Klett and Hassel [39] and Klett et al. [40]. After the welding process was completed, all the samples were immediately stored in liquid nitrogen. Then, the samples were heated to 400 °C for 30 min using a hot extraction analysis to determine the volume of diffused hydrogen. These data were used to calculate the amount of diffusible hydrogen by dividing it by the weight difference of the specimen before and after welding.

The inert gas fusion technique was used to quantify the O and H content in the weld metal and the metal droplets retained in the series of sieves used in the present study through a *LECO TCH 600* analyzer (LECO; *United States*). Samples of 500 mg were taken from the reinforcement of the weld beads. In addition, a sample was collected for each replication of the experimental design, guaranteeing three specimens for each combination of treatments. Concerning the metal droplets, three samples of 300 mg were analyzed for pulse frequency and constant current conditions. A
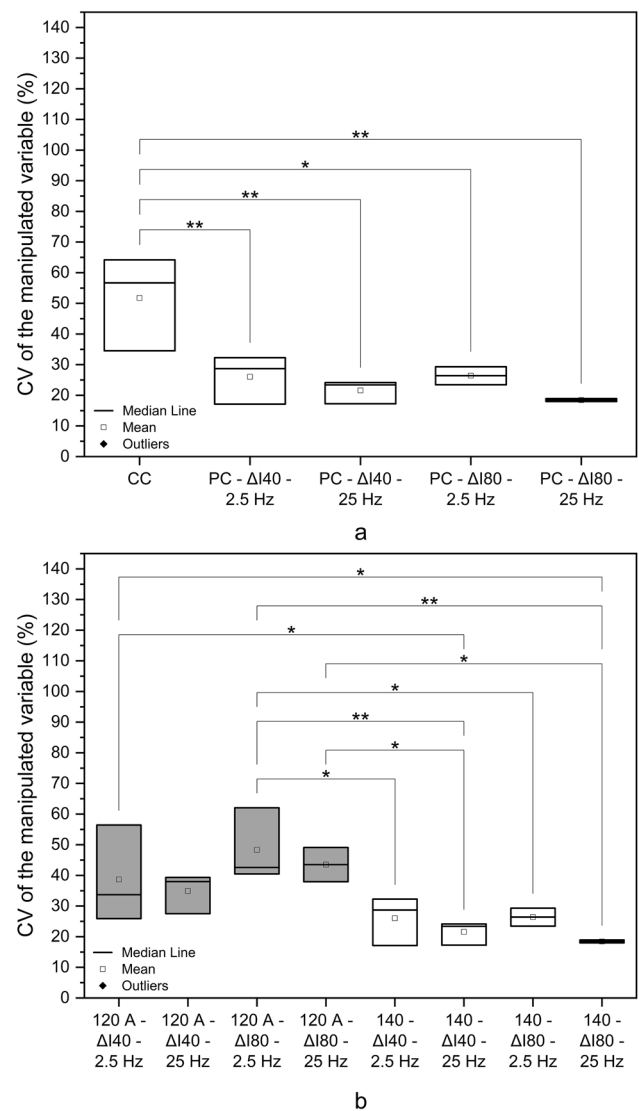
large chamber scanning electron microscopy was used for droplet composition analysis via energy dispersive analysis of X-rays (EDX) at the tip of the electrode.

3 Results and discussion

3.1 Operational performance of pulsed current vs constant current

Figure 8 illustrates the reaction of the system to the welding process parameters. There are two clear trends visible in the figure. The first shows greater significant electrode

oscillation at constant current while maintaining the target voltage (Fig. 8a). When comparing the results of pulsed current, no statistically significant differences can be found between the values of the ΔI and frequency factors for the 140 A mean welding current. The second trend is that the mean values of the coefficient of variation are higher for $I_m = 120$ A (Fig. 8b—gray box plots). This tendency was subjected to review through a multivariate linear regression model considering ΔI, I_m and frequency (CV—Coefficient of Variation of the manipulated variable as a response). For the experimental data, this model explains 65% of the variance (adj, $R^2 = 0.65$) with only I_m significantly influencing the outcome. It is expected because lower mean welding currents indicate lower arc energy, and thus lower process rigidity, generating poor stability (higher CV values). It is also important to point out that welding with a nominal current of 120 A and 35 V of the target voltage is hardly possible using the constant current power source and the automated system used. Therefore, the implementation of pulsed-current technology allows operation at lower current levels, which can be of interest for applications that require lower heat input, such as when dilution control is a critical factor. The superficial appearance of weld beads resulting from pulsed current with 120 A and 140 A mean welding currents are shown in Fig. 9. In the image, some spatter and differences in the weld bead width for the two experimental configurations can be noticed. Moreover, one can verify the greater penetration in the crater generated with 140 A mean welding current. No other welding defects are present.

For the lower values of the coefficient of variation with pulsed current and I_m 140 A, it can be concluded that the welding process is equalized with pulsed current, as detailed in Fig. 10. When welding with constant current, the oscillation of the current and voltage signals is a natural consequence of random metal transfer events, i.e., there is no control over the metal transfer process itself. On the other hand, in pulsed current, the arc voltage accompanies the modulation imposed by the current, as Scotti and Ponomarev [27] described in pulsed gas metal arc welding (GMAW). It is also interesting to note that the use of pulsed current possibly gives a periodicity to short-circuit events (blue arrows), as seen in the voltage oscillogram of Fig. 10. Similarly to Jia et al. [25], who applied pulsed current in underwater wet flux cored arc welding (FCAW), the process in pulsed current is more stable compared to the constant voltage mode, which resulted in electrical signals without significant violent disturbances.

In many industrial applications, random short circuits are avoided as a sign of instability and an unwanted operating parameter. However, as reported by Castellanos et al. [41], in some cases a higher short-circuit frequency results in a better performance of the process and a defect-free weld bead. On the other hand, Dutra [42] states that the pulsed-current
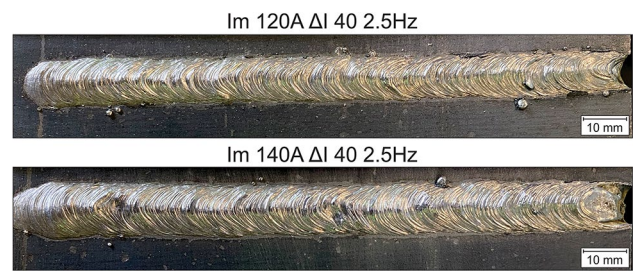

Fig. 9 Underwater wet welding beads generated with pulsed current at 0.5 m water depth

technique was conceived to enforce the transfer of the droplets avoiding the occurrence of short circuits. Figure 11a shows a slight tendency to obtain more short circuits in the pulsed-current condition. Furthermore, another difference between the experimental results in constant current and pulsed current is the fact that the open arc voltage is, on average, 0.3 V higher in constant current, as illustrated in Fig. 11b. Although the reference voltage is fixed at 35 V and the calculation of the average voltage of the process does not present significant differences, the factors of the experiment affect the average voltage during the electric arc periods. Indeed, the statistical model that defines open arc voltage as a response explains 73% of the variance (adj, $R^2 = 0.73$), highlighting ΔI and I_m as predictors. Figure 11c illustrates the relationship between the metal transfer period and the number of short circuits for the experimental data from the CC and PC tests. This result reinforces the trend that operating in pulsed current modulates the process voltage during arc periods and controls the frequency of metal transfer events. The aforementioned behavior had been seen for 120 A mean welding current.

It is important to recall that the experimental setup implemented in the present study used a PID controller to control the electrode feeding rate via AVC. To verify the possible influence of the response time of the control system on the performance of the system, Fig. 12 schematically shows the instantaneous variation of the welding current for a non-pulsed constant current process for shallow water depth. One can notice the increase in the current nominal value 30 s from the start of the welding process, i.e., through the displacement of the electrode (blue line). A more pronounced slope is evidenced on the right side of the graph, which corresponds to 180 A. Consequently, the change in current value increases the melting rate, so the process must control the target voltage by controlling the feed rate. Thus, the fed dynamic of the electrode changes, and the time in which the system tends to return to its stable state (feed rate of 11.2 ± 0.5 mm/s) can be related to the value of 2.4 s. Thus, combining the arc-voltage control system and pulsed-current
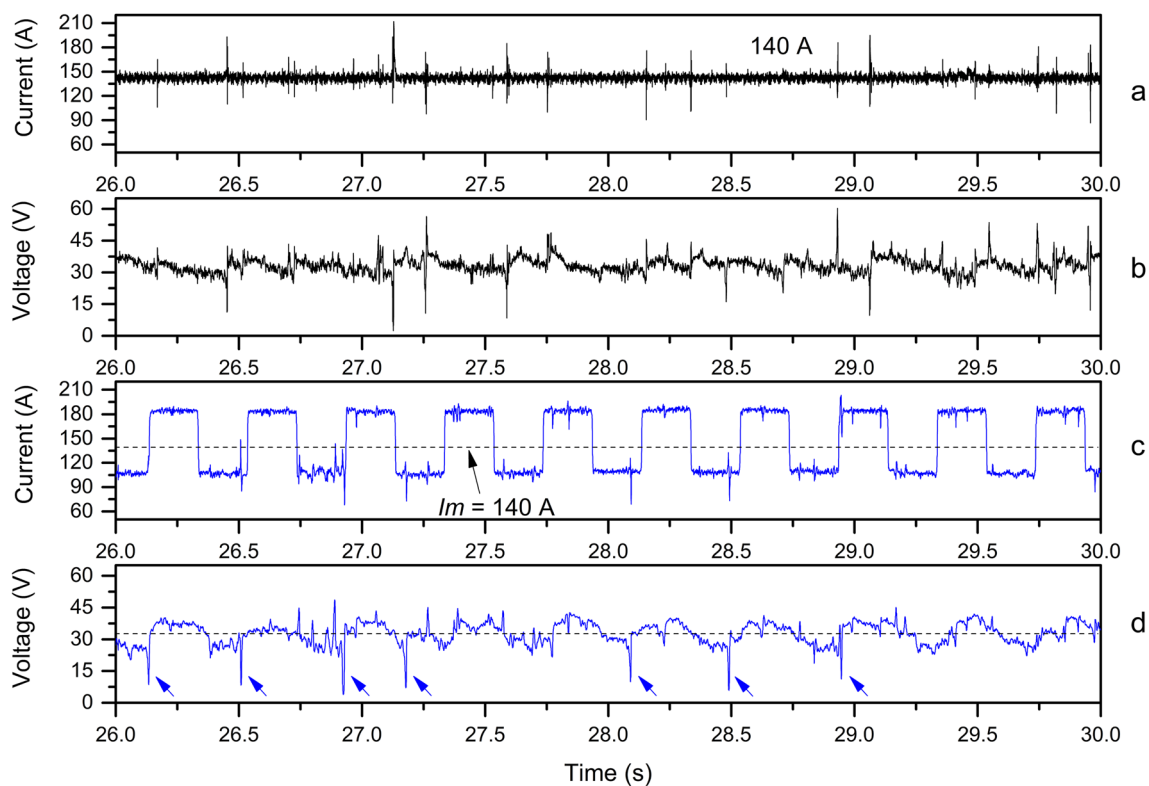
Fig. 10 Voltage and current welding oscillograms for constant current at 140 A (**a** and **b**) and pulsed current experimental condition at $I_m = 140$ A; $\Delta I = 80$; 2.5 Hz (**c** and **d**)

technology is the key factor in explaining the significantly higher number of short circuits.

It is important to note that there is a close interrelationship between the control system response time and the pulsed welding condition that influences the stability of the process. In fact, the non-operating points shown in Fig. 3 are possible in manual welding with the same electrode, welding parameters, and power source. On the other hand, by applying pulsed current, typical difficulties of the constant current process were overcome, such as problems of electric arc ignition and the extinction of the arc during the welding process. Similarly, Guo et al. [43] reported that in underwater FCAW, the duration of interruptions in the electric arc is reduced by applying optimized parameters in pulsed current.

Figure 13 illustrates the electrode feed and melting rate as a function of the experiment parameters. As expected, in the case of 140 A mean welding current (Fig. 13a), the pulsed current increased the feed rate of the electrodes. According to Modenesi and Uribe [12], it has been experimentally confirmed that the Joule effect significantly contributes to the higher fusion rate GMAW with pulsed current (P-GMAW) when compared to conventional GMAW for the same average current (nominal welding current in conventional GMAW $= I_m$ in P-GMAW). Applying similar reasoning,

Scotti and Ponomarev [27] explained that a melting rate increase of up to 15% is achieved with P-GMAW compared to GMAW short-circuit mode for the same average current. According to these authors, this is due to the fact that the effective current (I_{RMS}) of the pulsed wave is greater than that of the short-circuit welding wave. Hence, as is shown in Fig. 13b, there is a slight tendency to increase the mean current for higher ΔI, and in turn, as ΔI is increased, the values of I_{RMS} exhibit an increase surpassing those of I_m values. In this way, the I_{RMS} values help understand electrode consumption for the data presented in the present study. However, as described by Silva and Scotti [44], is important to point out that I_m and I_{RMS} constitute methods to represent the same electric current in relation to time.

From the data presented in Fig. 13c, it can be deduced that a higher level of I_m generates a higher melting rate, which is in line with general thinking. To prove that the difference observed for the melting rate was related to the difference in the mean welding current. The statistical model that defines melting rate as the response explains 80% of the variance (adj. $R^2 = 0.80$), presenting I_m as the statistically significant predictor.

It is also important to point out that both the melting rate and feed rate are related to electrode consumption. However, they were measured with different methodologies. The
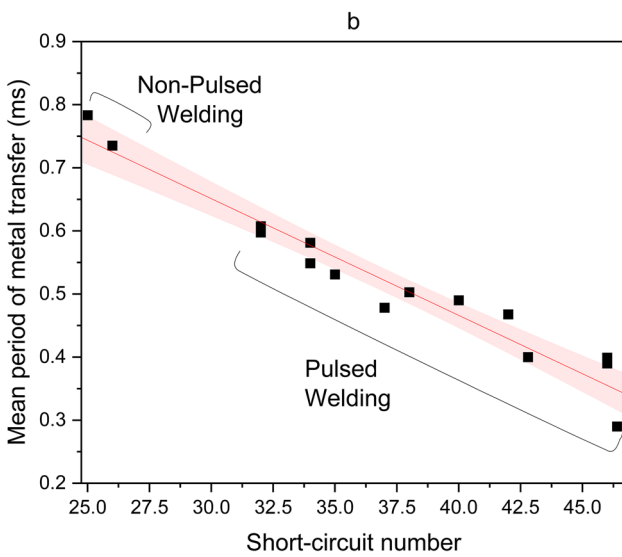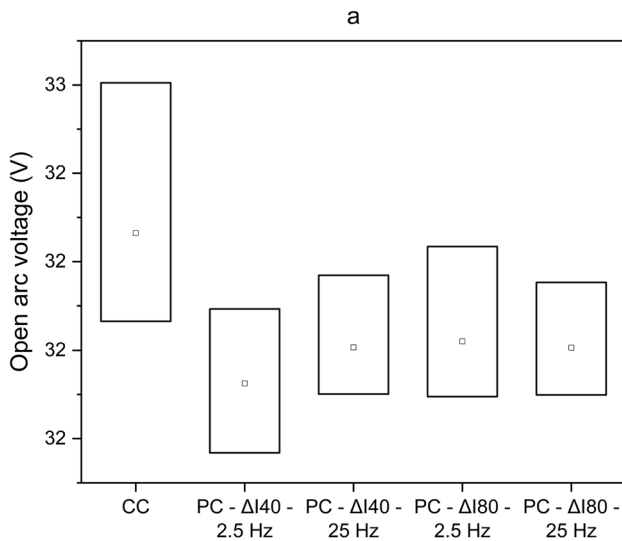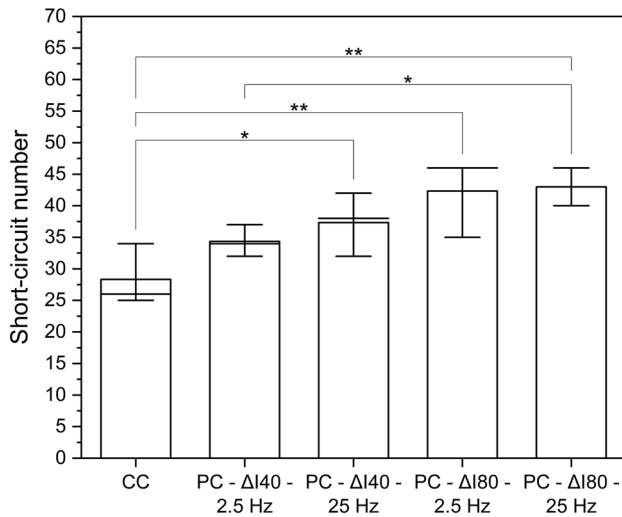
a

b

c

Fig. 11 Number of short circuits (**a**), open arc voltage (**b**), and mean period of metal transfer vs short-circuit number (**c**) comparing CC and PC for I_m 140 A; $*p \leq 0.05$, $**p \leq 0.01$, $***p \leq 0.001$
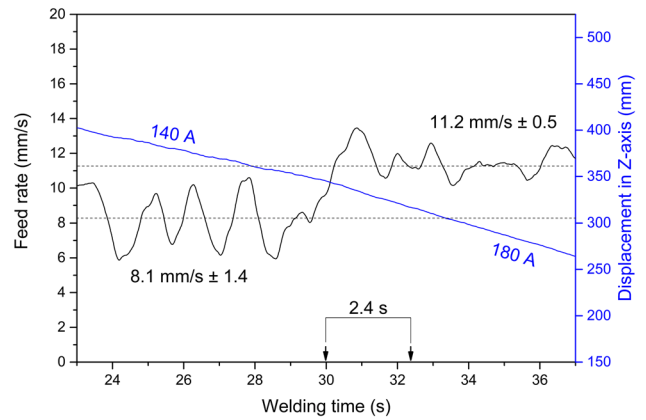

Fig. 12 Representation of the response time of the AVC system to an instantaneous current perturbance as a function of the feed rate

melting rate is a direct measurement of the consumption of the whole electrode, while the feed rate is an indirect measurement generated based on the feeding axis. Still, they are expected to be proportional. Regarding the first and second feed rate measurements, there is no evidence of a change in the fusion rate during electrode consumption for any of the study parameters.

Figure 14a quantitatively compares the use of conventional constant current and pulsed-current technologies on weld bead penetration. There is no statistically significant difference between the penetration resulting from the non-pulsed and pulsed current. Although I_{RMS} values are higher in pulsed current, penetration was not significantly affected. As already mentioned, the imposition of pulse periods and the welding system configuration resulted in a more significant number of short circuits. Thus, the non-existence of an electric arc due to the short-circuit phases results in a lower amount of energy that contributes to heating and melting of the base metal. Furthermore, if the two average current levels are compared (Fig. 14b), a higher weld bead penetration is expected for higher welding current levels. The influence of all experimental variables on penetration as an outcome was inspected using a multivariate regression model. Mean welding current (I_m), as the only significant influencing variable, resulted in a model that explains 75% of the variance. Finally, cross sections of weld beads relative to the experimental parameters investigated are shown in Fig. 15.

Regarding the influence of the pulsed current on the metal particle size and weight, Fig. 16 shows welding results at 140 A constant current and pulsed welding ($I_m = 140$ A $- \Delta I = 40$ A) with 2.5 Hz and 25 Hz pulse. The nominal opening size of the four sieves is displayed on the x-axis for all the graphs. Furthermore, the two smallest sieves (710 μm and 510 μm) were excluded from the results as they only accounted for 3% of the total weight. Thus, it is observed
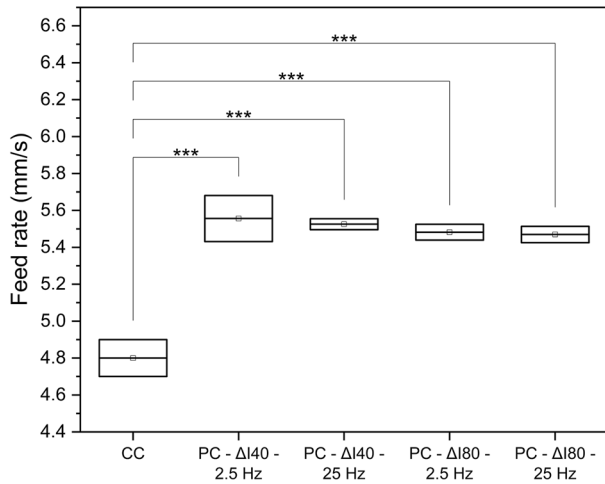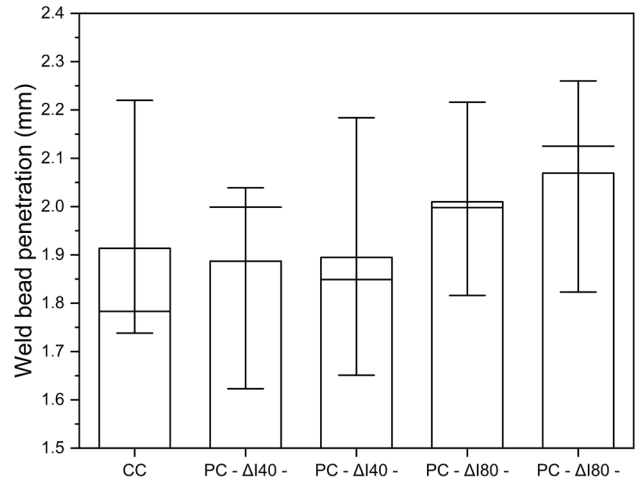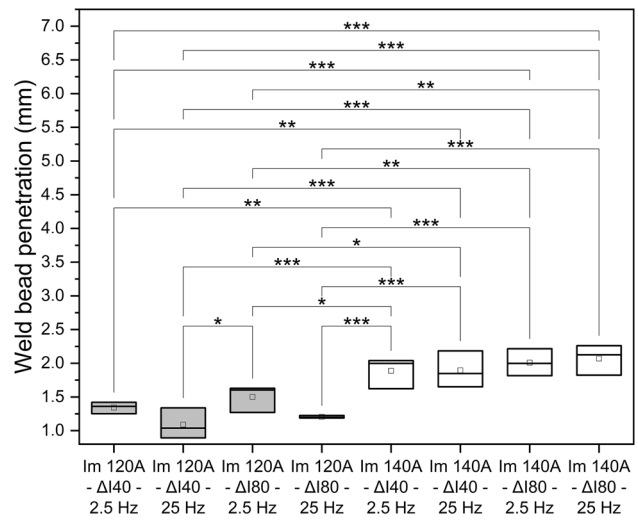
a
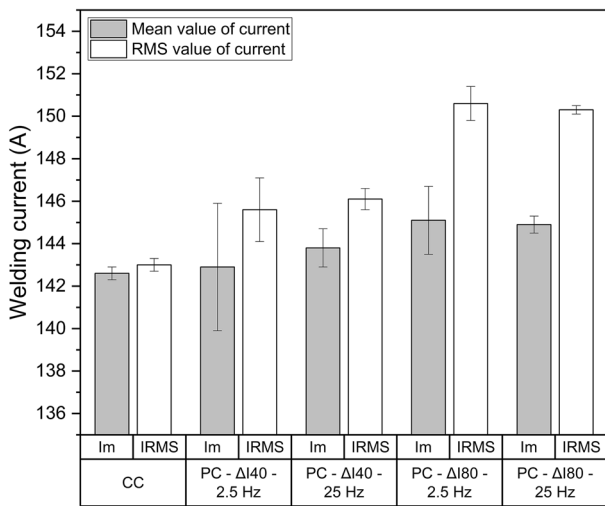
b
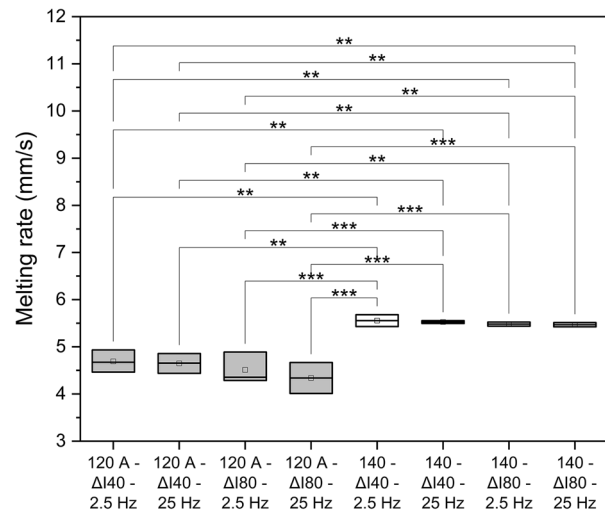
c

Fig. 13 Effect of pulsed current technology on the melting/feed rate: **a** CC vs PC on feed rate, **b** mean welding current vs root mean square (I_{RMS}) value of current, **c** 120 A vs 140 A on melting rate; $*p \leq 0.05$, $**p \leq 0.01$, $***p \leq 0.001$

a

b

Fig. 14 Weld bead penetration comparison between **a** CC vs PC and **b** 120 A and 140 A mean welding current; $*p \leq 0.05$, $**p \leq 0.01$, $***p \leq 0.001$

that for a 2.8 mm nominal sieve opening (Fig. 16a), the pulse frequency of 2.5 Hz results in a 40% lower weight of metal droplets than the constant current condition. In contrast to the constant current in non-pulsed welding, if the pulsed-current technology is used it results in a higher proportion of small metal droplets, as can be seen for the sieves of 1.0 mm, 1.4 mm, and 2.0 mm (Fig. 16a). Likewise, the number of droplets (Fig. 16b) supports those above results since pulsed welding produces more metal droplets for the 1.0 mm, 1.4 mm, and 2.0 mm sieves than the constant current condition. Jia et al. [25] noted that using pulsed current in underwater FCAW resulted in smaller droplet sizes and higher transfer frequency as compared to conventional wet FCAW. In addition, Deyev and Deyev [18] mention that droplet dimensions

Fig. 15 Cross sections of the weld generated with pulsed current
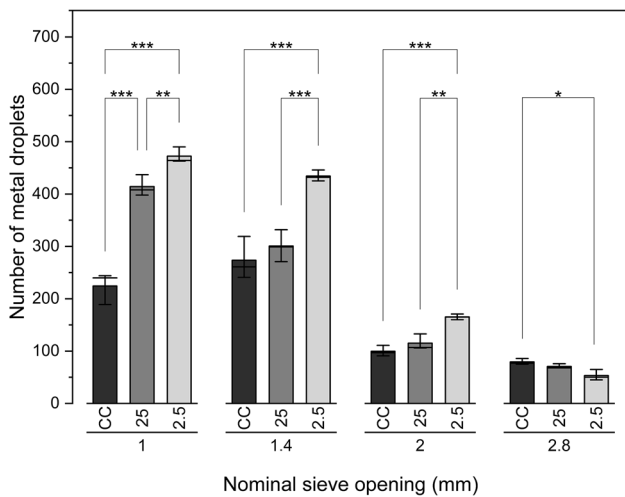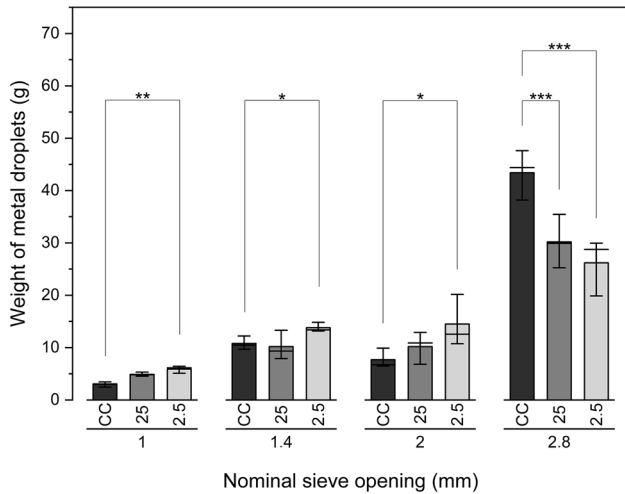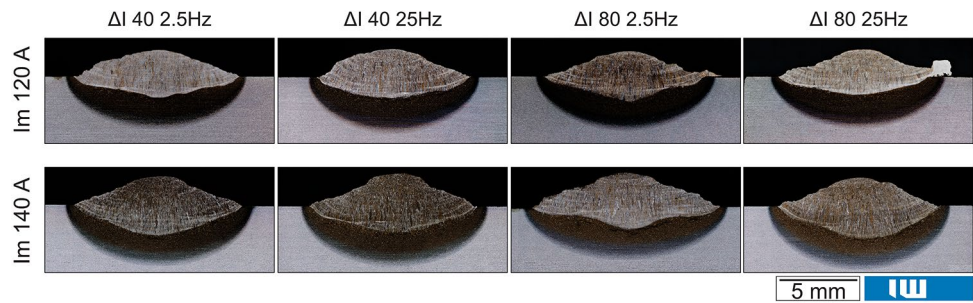

Fig. 16 Weight and number of metal droplets as a function of the metal droplet size distribution for constant current and pulsed welding (I_m140A—ΔI40); *$p \leq 0.05$, **$p \leq 0.01$, ***$p \leq 0.001$

depend on welding current, i.e., a rise in current density results in a significant decrease in the weight of the metal droplets. Therefore, one can infer that the electromagnetic

forces produced during the pulse period force the metal transfer with a high amount of droplets. Xu et al. [45], using droplet size distribution analysis, also noted that an increase in welding current results in an increase in the number of droplets.

As illustrated in Fig. 17, for a nominal current of 140 A in constant current mode, the growth of the metal droplet at the tip of the electrode is evident (Fig. 17a) and its subsequent detachment (Fig. 17b). Thus, voltage oscillations and process behavior are natural consequences of metal transfer events. In addition, the irregular detachment of freely flying droplets (free-flight metal transfer) also significantly impacts arc-voltage fluctuations [12], as seen in Video 1 (see supplementary material).

On the other hand, Fig. 17c and d (Video 2) compare the pulse period and the base current for an experiment with a frequency of 25 Hz, $\Delta I = 80$ A, and 140 A mean welding current I_m. In addition to the apparent difference in luminosity and volume of the electric arc, one can note singularities in the metal transfer phenomenon. Looking at Fig. 17c, there is a droplet growing on the tip of the electrode as another metal droplet reaches the weld pool. On the other hand, during the pulse period, violent droplet transfer is evidenced as a consequence of the higher electromagnetic forces, a more intense and robust plasma arc as compared to the conventional mode of operation, and a higher stirring of the welding pool, as shown in Video 2. Furthermore, during the pulse phase, the acceleration of the detached metal droplet is very high [27], possibly reducing the travel time of the droplet through the plasma volume and impacting the weld pool at high speeds. Also, Jia et al. [25] noted that metal particles are accelerated during the pulse period in underwater FCAW.

3.2 Influence of pulsed welding on underwater welding chemistry

Figure 18a shows the oxygen content of the droplets distributed between the 1.0 and 2.8 mm sieves. The experimental results confirm that the metal droplets have a higher oxygen content for the constant current condition mode. A

Fig. 17 Particularities in metal transfer from a covered electrode for non-pulsed SMAW (**a** and **b**) and pulsed SMAW ($I_m = 140$ A; $\Delta I = 40$ A; 25 Hz) during the base current (**c**) and pulse period (**d**); nominal and mean welding current value are equal to 140 A; onshore condition
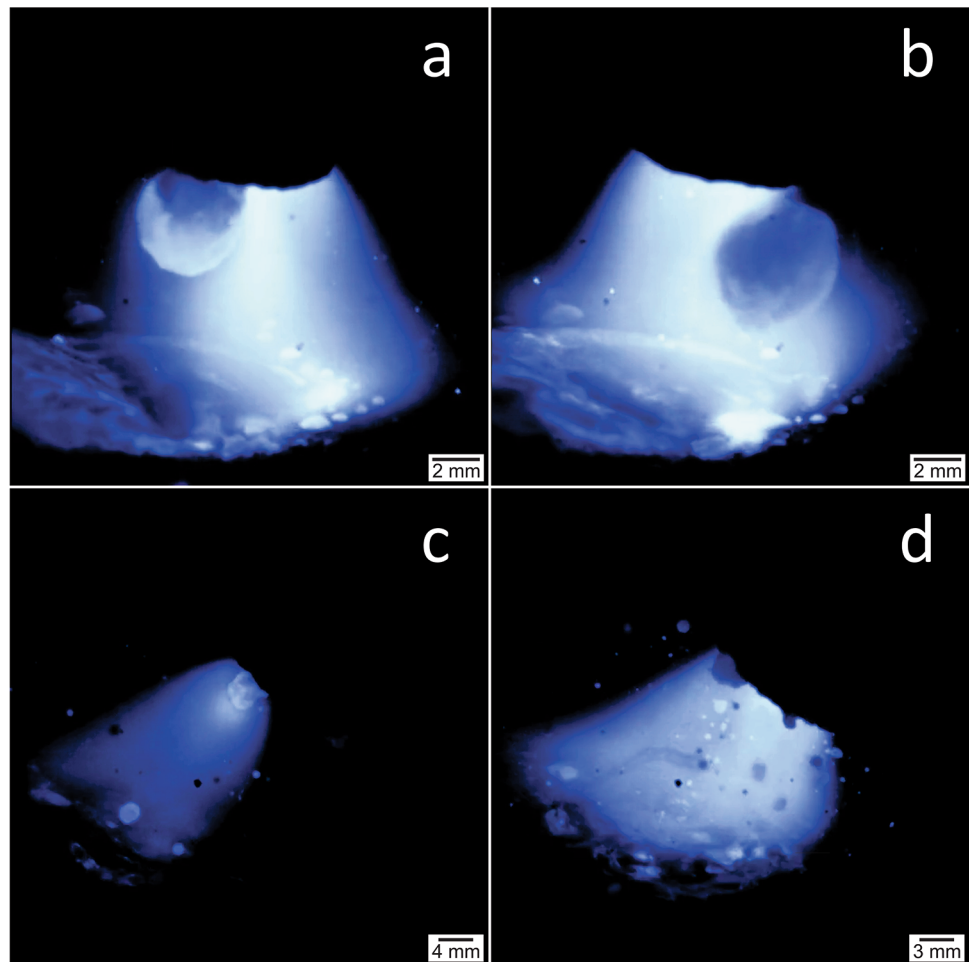
similar behavior is seen in Fig. 18b, in which the residual hydrogen content is lower for the metal droplets generated with the pulsed current. This indicates a strong influence of pulse technology on the composition of the metal droplets. In addition, it is important to notice that smaller metal droplets result, in general, in a higher content of oxygen and residual hydrogen.

Figure 19 shows the cross-section of metal droplets collected from 1.0 mm and 2.8 mm mesh openings for pulsed welding. Larger particles have an internal pore, while the pore is not in smaller droplets. Similar results were obtained by Brandi et al. [20], who mentioned that internal porosity is exhibited only in the largest droplets. Considering cross sections of droplets were produced under constant current and pulsed-current conditions (140A – ΔI40A – 2.5 Hz), *ImageJ* software was used to measure the external diameter of the droplet and the pore diameter for the 2.0 mm and 2.8 mm mesh openings. For each experimental condition and sieve, 20 droplets were measured. Assuming that all the droplets are spherical, Table 3 shows the volume of the droplets and the volume of the pore as a function of the experiment parameters.

Thus, for droplets collected from the constant current condition experiments, the pore volume represents approximately 50% of the volume of the metal droplet for the 2.8 mm particle size distribution. In contrast, at 2.0 mm, it represents 34%. On the other hand, the pores inside the droplets collected from pulsed welding represent 19% and 24% for 2.0 mm and 2.8 mm particle size distribution, respectively. Considering the previous results, it is probable that the constant current droplets carry a larger volume of gases in their interior compared to the experimental condition of pulsed welding.

The higher dissolved gas content in the small metal droplets is justified by the specific surface area. Considering that the specific surface area can be expressed as area per volume (m^2/m^3), as Ghasemi et al. [46] described, the specific surface area increases with decreasing particle size (r, radius), as shown in Eq. 1. In this way, the surface activity and adsorption volume change according to the specific surface area, justifying that the dissolved gas content should be higher for smaller droplets. It is essential to remark that larger droplets probably carry more gases under typical underwater welding conditions since the total gaseous compounds comprise the pore volume within
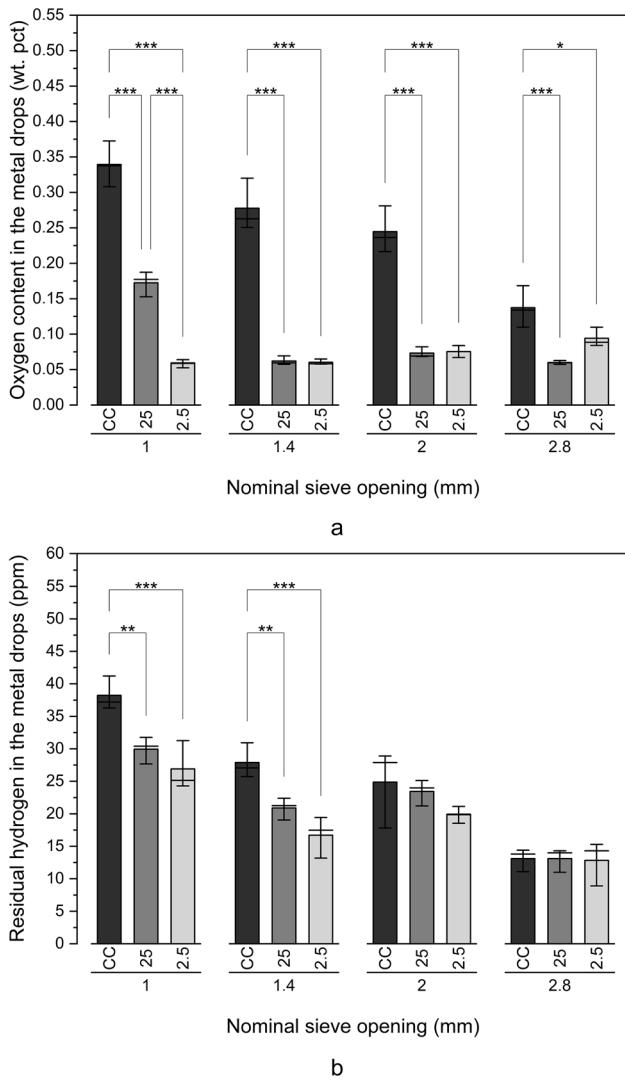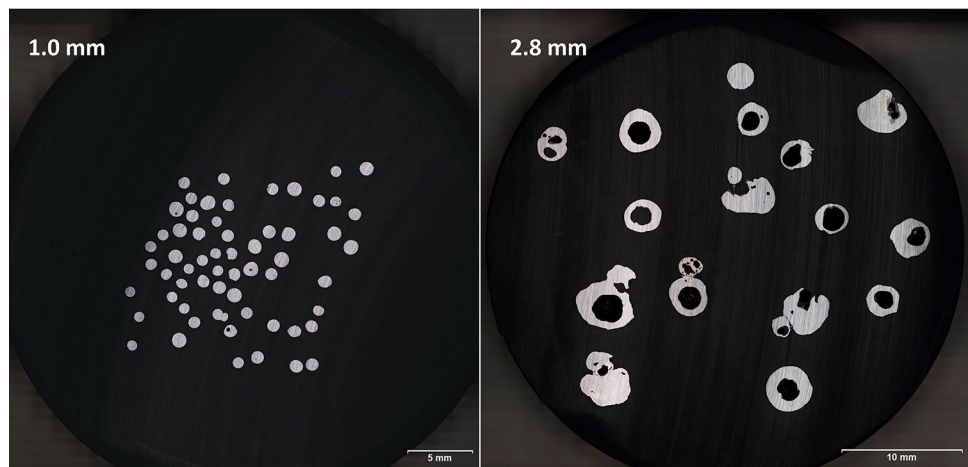
Fig. 18 Oxygen and residual hydrogen content as a function of the metal droplet size distribution for constant current and pulsed welding (I_m140A–ΔI40); *$p \leq 0.05$, **$p \leq 0.01$, ***$p \leq 0.001$

Fig. 19 Cross section of metal droplets resulting from the pulsed-current condition: 140 A mean welding current, ΔI 40 A and 2.5-Hz

the droplet and the species dissolved in the metal, as Guo et al. [47] suggested.

$$\frac{\text{Surface}}{\text{Volume}} = \frac{4\pi r^2}{\frac{4}{3}\pi r^3} = \frac{3}{r}. \tag{1}$$

The discussion above was focused mainly on the effect of the welding condition on the oxygen and residual hydrogen content in the metal droplets without considering the order of magnitude obtained experimentally in the analytical elemental analysis of the unwelded material. As for the metal droplets, a maximum of approximately 0.35 wt% oxygen is reported; for the base metal (S355J2) and the electrode core wire, the oxygen content according to the composition statement is 0.015 wt% and 0.025 wt%, respectively. This comparison indicates that the oxygen contents in the metal droplets are too high to consider only the dissolved oxygen in the iron matrix and the oxygen-rich inclusions within the metal. Santos [48] reported 0.25 wt% as the solubility limit of oxygen in liquid iron for temperatures of 1600 °C. For a temperature relatively closer to that reported for the metal droplet (2046 °C), the solubility of oxygen in liquid iron can be calculated from the work of Fischer and Schumacher [49], resulting in 1.82 wt%. However, the authors' experiments were carried out through the levitating melting method, which is not entirely comparable with the welding system. Moreover, considering the influence of coating ingredients, such as Al, Ti, Si, and Mn (as reported by Hazlett) [50], the solubility value should be closer to that reported by Santos [48]. Considering the above, if the results for oxygen in metal droplets included slag adhered to the surface of the droplets, part of the relationship between droplet size and oxygen content would be substantiated. However, the separation between droplets and slag was performed by mechanical vibration (as seen in the methodology section).

On the other hand, Pope [51] discussed formation of an FeO film on the surface of metal droplets and the weld pool due to a kinetic reaction between water and liquid iron. This

Table 3 Metal droplet morphological characteristics in pulsed and constant current welding condition

Characteristic	Welding condition			
	Constant current welding		Pulsed welding	
Mesh (mm)	2.0	2.8	2.0	2.8
Mean metal droplet diameter (mm)	2.0 ± 0.2	3.8 ± 0.5	2.1 ± 0.3	2.9 ± 0.2
Mean pore diameter (mm)	1.4 ± 0.1	3.0 ± 0.5	1.2 ± 0.2	1.8 ± 0.2
Metal droplet volume (mm^3)	33.5	229.8	38.8	102.2
Pore volume (mm^3)	11.5	113.1	7.2	24.4
Volumetric ratio (%) *	34	49	19	24

*Ratio of pore volume to metal droplet volume

reaction occurs mainly for electrodes of an oxidizing nature (high concentrations of hematite in the coating); however, the highly oxidizing medium found in underwater welding would favor the conditions for forming an ionic monolayer of oxygen atoms. Figure 20a shows data from EDX analyses performed for metal droplets anchored in the arc barrel of the electrode tip. These droplets resulted at the end of bead-on-plate welds. Using the elemental composition mapping technique, the Fe, O, Si, Ca, Ti, and Mn concentrations are observed and can be qualitatively evaluated. As seen in Fig. 20b, oxygen is present almost exclusively on the metal droplet, indicating the possible formation of the FeO layer. This way, the greater surface area per mass of metal in the metal droplets and the FeO layer adhered to their surface would justify oxygen contents higher than the reported solubility limit.

Furthermore, it is interesting to point to the elemental migration of manganese, which is distributed on the metal droplet and slag. Manganese is a well-known deoxidizer used to control the final oxygen content of metal droplets [52] and weld metal. Also, in the composition maps it is possible to identify regions with a particularly high content of Si, Ca, and Ti (marked by the white arrows). This would be the interface between the metal droplet and the molten coating slag.

Furthermore, experimental evidence provided by Grong [14] hints at a possible mechanism that results in high-oxygen content in the metal droplets. Based on observations by Corderoy et al. [53], there is a re-dissolution of the slag (formed during the growth stage of the droplet at the tip of the electrode) in the superheated metal during the droplet's travel through the arc gap, resulting in high oxygen concentration. The above mechanism could explain (at least partially) the lack of slag on the underwater metal droplet surface, as observed by Guo et al. [47]. Also, it is possible that the high-cooling rates generated by the application of the droplet collector technique (similar device to the one developed in the present study) would freeze the chemical species in the metal droplets, preserving the established composition at high temperatures [14].

3.3 Pore formation in the metal droplet

Figure 21 presents an idealized model of the dynamics of absorption and evolution of gases in the pore inside the metal droplets. Note that the stages of the model are assembled on a graph of solubility vs temperature for iron. The main difference between this model and the plot from Tomić et al. [54] and Engel and Klingele [55] is that the model shown in the present study adopts the maximum temperature reported for the metal droplets, i.e., 2400 K [51]. Meanwhile, in fusion-welding process, Deyev and Deyev [18] mentioned that liquid metal dissolves a specific quantity of gas during welding. Many of these gases constitute the atmosphere of the electric arc, and they are the product of the fusion of various coating elements [12] and, in the specific case of underwater welding, the breakdown of the water molecule. According to Modenesi et al. [15], both the gases and the molten metal are violently heated by the electric arc, creating highly favorable conditions for developing physical and chemical interactions between the molten metal and the surrounding environment. These interactions are particularly intense in the small droplets of molten metal formed from the consumable electrode. Thus, in the first stage and through diffusion and convective flows (see Fig. 22), according to Deyev and Deyev [18], the alloying components in the metal droplets chemically react with oxygen, while hydrogen is dissolved in the metal.

In the second stage, the metal droplet traveling through the arc column undergoes thermochemical reactions by superheating, and there is nucleation, growth, and coalescence of gaseous products (as described by Bøjesen and Iversen) [56]. In this way, the gases (atoms, molecules, or ions) react with each other, and the gas volume expansion occurs inside the metal droplet due to temperature and pressure gradients and the interaction between the electric arc and the molten droplet, as seen in video 3. As noted by Xu et al. [45], the reactions of the gases generated from the electrode favor the growth of the gas bubble inside the droplet of molten metal.
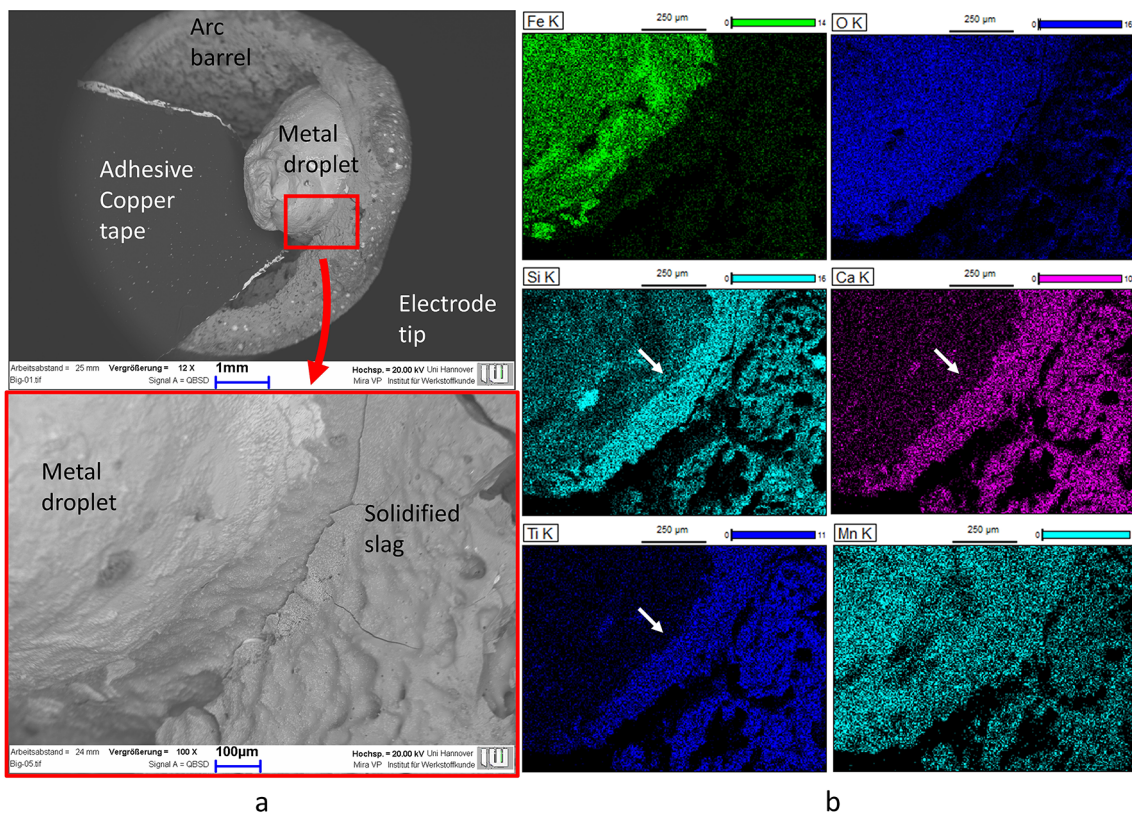
Fig. 20 **a** SEM micrographs of the metal droplet at the electrode tip and **b** elemental mappings (EDX) of the metal droplet and slag
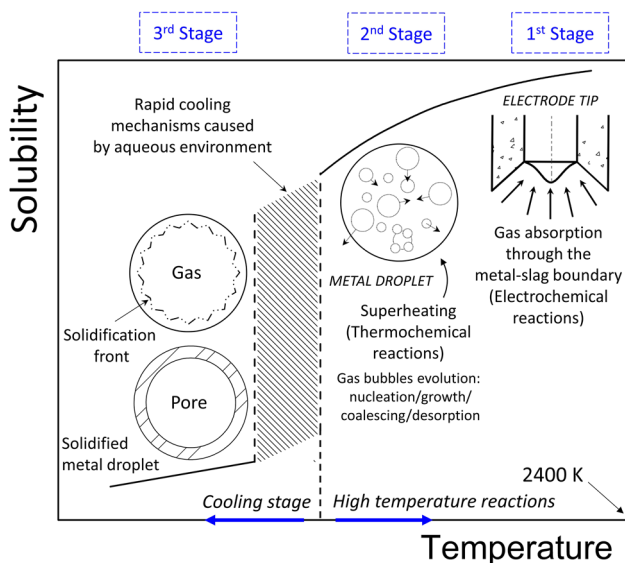

Fig. 21 Mechanism of formation of pores in metal droplets as a function of solubility and temperature based on the overall reaction model by Grong [14]

According to Deyev and Deyev [18], eliminating gases from the metal can occur through surface desorption or generation of a gas bubble within the molten metal, facilitating the degassing process. In Fig. 21, those first two stages are grouped into the high-temperature stage, where elements are absorbed extensively into the liquid metal.

Subsequently, during the cooling stage (3rd stage in Fig. 21), the temperature drops quickly from values close to the boiling temperature of the liquid metal droplet to its solidification temperature at the solid–liquid interface. The subcooling conditions to which the metal droplet is subjected contribute to a decrease in solubility of certain species, leading to a rapid increase in supersaturation, as Grong [14] mentioned. For instance, the solubility of hydrogen decreases rapidly during the solidification process.

This way, the gases intensely absorbed in stages 1 and 2 can become supersaturated in stage 3. Finally, the solidified metal can trap the gas bubble, forming a pore. Figure 22 shows a schematic of the gas–metal interactions in the metal droplet for covered electrodes in underwater welding. Furthermore, one can note that there are similarities between the model presented in this study and the porosity formation mechanism in weld beads.

3.4 Content of H and O in the weld metal

Figure 23a illustrates the diffusible hydrogen content in the weld metal for three experimental conditions. There is no

statistically significant difference between the hydrogen values reported by Klett and Hassel [39] (diffusible hydrogen value in constant current) and values measured in welds welded with a pulse frequency of 2.5 Hz. In contrast, the 25 Hz frequency results in higher diffusible hydrogen content. The oxygen content in the weld metal shows a similar trend, as seen in Fig. 23b.

Considering the previous results and the analyses developed in the present study, it is possible to infer that even though the application of pulsed-current technology affects the metal transfer particle size distribution, there is no effect on the diffusible hydrogen content. However, this hypothesis is valid exclusively for the experimental conditions in the present study since pulsed-current technology provides a large spectrum of parameters that can be configured (which at the same time is the most significant limitation of this control method of the welding process, as stated by Castellanos-Gonzalez et al.) [57]. Thus, it is likely that another phenomenon not elucidated in the present study is responsible for the diffusible hydrogen content. It is speculated that under the experimental conditions employed, the region of the weld pool is probably a gas species critical absorption spot due to the increased stirring of the molten metal because of the pulse period. Indeed, as reported by Grong [14], as a consequence of intense turbulence in the weld pool, large amounts of oxygen are absorbed, resulting in a significant loss of deoxidizers [58]. In addition, the author mentions that a more extended-weld-pool interaction time
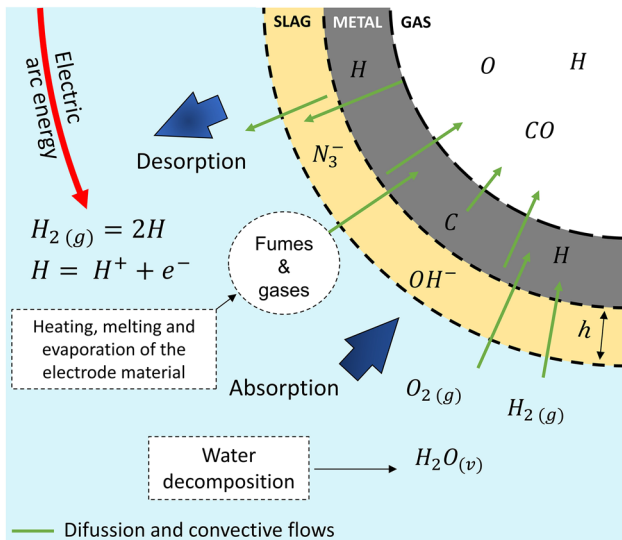

Fig. 22 Idealized scheme of entering/leaving species in the metal droplet reaction zone; although of essential importance for oxide removal and shaping of the weld pool chemistry, this model does not consider the interactions between the molten metal and the slag; h = thickness
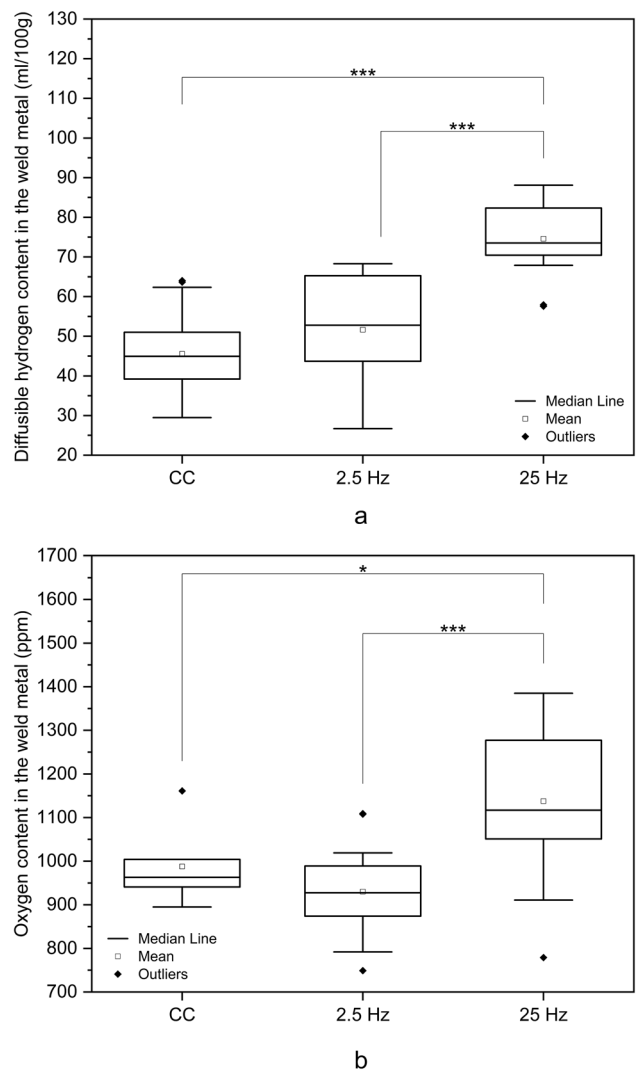

Fig. 23 Diffusible hydrogen (**a**) and oxygen content (**b**) for pulsed welding ($I_m = 140$A) and constant current conditions ($I = 140$A); *$p \leq 0.05$, **$p \leq 0.01$, ***$p \leq 0.001$

favors oxygen absorption compared to droplets at the tip of the electrode.

As seen in Video 2, the weld-pool stirring could be related to the increased pressure and force resulting from the stronger plasma during the pulse period. Likewise, the 25 Hz frequency probably imposes a gas flow regime in the electric arc, different from that derived from constant current and at the lower pulse frequency. According to Pope [51], welding parameter changes strongly influence the final oxygen content in the weld metal. This way, the change between peak and base current creates local turbulent conditions in the electric arc environment (gas bubbles), resulting in greater gas absorption in the molten metal.

Along this line of reasoning, the diffusible hydrogen content for the pulsed-current condition at 120 A mean welding current is shown in Table 4. There is no difference

in the content of diffusible hydrogen in the weld metal for the experimental conditions described. It is assumed that the higher instability of this configuration (as seen in Fig. 8) probably generates intense turbulence, resulting in a higher uptake of gaseous species in the weld metal. The described mechanism could lead to a higher diffusible hydrogen and oxygen content in the weld metal.

Recently, Guo et al. [47] pointed out that the inappropriate distribution of slag around the metal droplet is probably the pathway for hydrogen to enter the molten metal. The authors stated that replacing calcium fluoride with rutile and adopting a filling rate of 28% in 1.6-mm diameter experimental tubular wires guarantees a higher formation of protective slag around the surface of the metal drop, which results in lower diffusible hydrogen contents in underwater welds.

4 Conclusions

This exploratory study shows that pulsed-current technology with covered electrodes is beneficial for underwater welding. This is a starting point for future works investigating the many variables involved in this approach since, as with any welding, the choice of parameters consists of a trade-off between the need for stability and the resulting properties of the weld, such as the geometry, dilution of the base metal, hardness, and welding metallurgy. The main findings can be summarized as follows:

- the use of pulsed-current results in a more stable welding process compared to the constant current mode;
- implementing pulsed welding technology allows operating at lower mean welding current levels than in constant current mode and higher melting rates can be obtained through pulsed current;
- the implementation of a pulsed-current period in wet SMAW leads to significantly higher number of metal droplets with smaller diameters compared to the constant current condition;
- the pulse period probably modifies the velocity of the metal droplets traveling through the plasma, possibly decreasing the interaction time of the molten metal with the surrounding environment;
- metal droplets collected using a constant current welding source result in a higher residual hydrogen and oxygen content as compared to pulsed-current technology;
- the constant current metal droplets carry a larger volume of gases in their interior compared to the pulsed-current condition;
- there is no statistically significant difference between the diffusible hydrogen content of welds in constant current

Table 4 Diffusible hydrogen in the weld metal for 120 A mean welding current in pulsed welding

Pulsed welding condition	Diffusible hydrogen content (ml/100 g)	
	Mean	Standard deviation
ΔI40–2.5 Hz	107.5	47.6
ΔI40–25 Hz	108.9	32.2
ΔI80–2.5 Hz	99.5	39.8
ΔI80–25 Hz	106.1	44.2

and values measured in welds welded with a pulse frequency of 2.5 Hz.

Author contributions Andrés M. Moreno-Uribe: conceptualization, methodology, software, formal analysis, investigation, data curation, writing—original draft, visualization. Leandro Vaccari: validation, writing—review and editing. Alexandre Q. Bracarense: writing—review and editing. Hans J. Maier: writing—review and editing, resources. Thomas Hassel: writing—review and editing, resources, supervision. All authors read and agreed upon the final version of the manuscript.

Data availability The data that support the findings of this study are available on request from the corresponding author.

Declarations

Conflict of interest The authors declare that they have no known competing financial interests or personal relationships that could have appeared to influence the work reported in this paper.

References

1. Pessoa EP, Liu S. The state of the art of underwater wet welding practice: part 1. Weld J. 2021;100:132–41. https://doi.org/10.29391/2021.100.011.

2. Pessoa EP, Liu S. The state of the art of underwater wet welding practice: part 2. Weld J. 2021;100:171–82. https://doi.org/10.29391/2021.100.014.

3. Assunção MT, Bracarense AQ. A novel strategy to improve melting efficiency and arc stability in underwater FCAW via contact tip air chamber. J Manuf Process. 2023;104:1–16. https://doi.org/10.1016/j.jmapro.2023.08.054.

4. Lara RF, Uribe AMM, Bracarense AQ. Development of a hatch system for the determination of diffusible hydrogen in underwater welding. Respuestas. 2020;25(1):18. https://doi.org/10.22463/0122820X.2433.

5. Jamrozik W, Górka J. Assessing MMA welding process stability using machine vision-based arc features tracking system. Sensors. 2021;21(1):84. https://doi.org/10.3390/s21010084.

6. Fydrych D, Tomków J. Underwater processing of materials. Materials. 2022;15(14):4902. https://doi.org/10.3390/ma15144902.

7. Amaral EC, Jácome-Carrascal JL, Moreno-Uribe AM, Bracarense AQ. Influence of the formulation of a flux-cored wire on the microstructure and hardness of welded metal. J Phys. 2021;2118(1): 012010. https://doi.org/10.1088/1742-6596/2118/1/012010. (**IOP Publishing**).

8. Uribe AMM, González OMC, Botia GCP, Carrascal JLJ, Rodríguez A. manufactura de alambre tubular autoprotegido y evaluación de condiciones operacionales en soldadura submarina. Investigación e Innovación en Ingenierías. 2021;9(1):167–79. https://doi.org/10.17081/invinno.9.1.4015. (**Spanish**).

9. Fydrych D, Świerczyńska A, Rogalski G. Effect of underwater wet welding conditions on the diffusible hydrogen content in deposited metal. Metallurgia Italiana. 2015;11(12):47–52.

10. Fydrych D, Raczko P, Świerczyńska A, Landowski M, Wolski A, Rogalski G. Effect of arc strikes on high strength low alloy steels welded by SMAW. Adv Sci Technol Res J. 2023;17(3):160–9. https://doi.org/10.12913/22998624/166061.

11. Solano JLO, Moreno-Uribe AM, Jaimes BRA, Okuyama MP, Arias AR. Detection and characterization of metal transfer in GMAW using computational vision algorithms. Int J Adv Manuf Technol. 2023;128(7):3415–25. https://doi.org/10.1007/s00170-023-12180-9.

12. Modenesi PJ, Uribe AMM. Introduction to the physics of the electric arc and its application to the welding of materials. Bogotá: Ecoe ediciones; 2022. (**ISBN: 978-958-503-296-5**).

13. Ortiz JL, Moreno-Uribe AM, Acevedo BR, Lima EJ, Arias AR. Application of computer vision techniques for contour detection in underwater wet welding: an exploratory study. J Phys. 2021;2046(1): 012072 (**IOP Publishing**).

14. Grong Ø, Grong D. Metallurgical modelling of welding, vol. 2. London: Institute of materials; 1997.

15. Modenesi PJ, Marques PV, Santos DB. Introdução à metalurgia da soldagem. Belo Horizonte: UFMG. Portuguese. 2012. Retrieved November 13, 2023, from https://demet.eng.ufmg.br/wp-content/uploads/2012/10/metalurgia.pdf

16. Quintana Puchol R, Perdomo González L, Duffus Scott A, Bracarense AQ, Pessoa ECP. Consideraciones termodinámicas entre la formación de poros y la presión hidrostática durante la soldadura subacuática mojada. Soldagem Inspeção. 2009;14:161–9. https://doi.org/10.1590/S0104-92242009000200008. (**Spanish**).

17. Quintana Puchol R, Perdomo-González L, Bracarense AQ, Pessoa ECP. Valoración termodinámica de la descomposición del vapor de agua a 1 atmósfera por la acción de un arco eléctrico y solubilidad del hidrógeno en hierro líquido. Afinidad. 2009;66(542):320–5. (**Spanish**)

18. Deyev GF. Surface phenomena in fusion welding processes. Boca Raton: CRC Press; 2006.

19. Larson LJ. Metal transfer in the metallic arc. Weld J. 1942;21(2):107s.

20. Brandi SD, Taniguchi C, Liu S. Analysis of metal transfer in shielded metal arc welding. Weld J. 1991;70(10):261s-s270.

21. Pérez-Guerrero F, Liu S. Explaining porosity formation in underwater wet welds. Int Conf Offshore Mech Arctic Eng. 2007;42703:249–57. https://doi.org/10.1115/OMAE2007-29696.

22. Pessoa ECP. Estudo da variação da porosidade ao longo do cordão em soldas subaquáticas molhadas. Doctoral thesis. Federal University of Minas Gerais. Portuguese. 2007.

23. Turani CV. Influência do polímero utilizado como aglomerante em eletrodos revestidos básicos sobre a formação de ferrita acicular no metal de solda. Doctoral thesis. Federal University of Minas Gerais. Portuguese. 2014.

24. Xu C, Guo N, Zhang X, Chen H, Fu Y, Zhou L. Internal characteristic of droplet and its influence on the underwater wet welding process stability. J Mater Process Technol. 2020;280: 116593. https://doi.org/10.1016/j.jmatprotec.2020.116593.

25. Jia CB, Wu J, Han YF, Zhang Y, Yang QY, Wu CS. Underwater pulse-current FCAW-part 1: waveform and process features. Weld J. 2020;99(5):135–45. https://doi.org/10.29391/2020.99.013.

26. Richardson IM, Bucknall PW, Stares I. The influence of power source dynamics on wire melting rate in pulsed GMA welding. Weld J. 1994;73:32-s.

27. Scotti A, Ponomarev V. Soldagem MIG/MAG: melhor entendimento, melhor desempenho. São Paulo: Artliber editora. Portuguese; 2008.

28. Finsterwalde K. Schweißelektroden Handbuch. Niederlausitz: Kjellberg Finsterwalde Elektroden und Zusatzwerkstoffe GmbH. German; 2019.

29. Montgomery DC, George CR. Applied statistics and probability for engineers. John Wiley & Sons; 2018. (**ISBN: 978-1-119-40036-3**).

30. Uribe AMM, Bracarense AQ, Pessoa ECP, dos Santos VR. Influência da Polaridade Sobre a Estabilidade do Processo de Soldagem Subaquática Molhada com Eletrodo Revestido. Soldagem Inspeção. 2017;22(4):429–41. https://doi.org/10.1590/0104-9224/SI2204.13.Portuguese.

31. Pistorius PGH, Liu S. Changes in metal transfer behavior during shielded metal arc welding. Weld J-Include Weld Res Suppl. 1997;76(8):305–15.

32. Bracarense AQ, Liu S. Chemical composition variations in shielded metal arc welds. Weld J. 1993;72(12):529s–36s.

33. Liberato FDM, Modenesi PJ, Bracarense AQ. Aspectos Operacionais da Soldagem Subaquática Molhada com Eletrodos Revestidos Inoxidável Austenítico. Soldagem Inspeção. 2018;23:277–91. https://doi.org/10.1590/0104-9224/SI2302.13.Portuguese.

34. Ghosh PK. Pulse current gas metal arc welding. New York: Springer; 2017. https://doi.org/10.1007/978-981-10-3557-9.

35. Modenesi PJ, Costa MCMDS, Santana IJ, Berganholi JPP. Estudo de alguns parâmetros básicos da soldagem GMAW com transferência por curto-circuito. Soldagem Inspeção. 2011;16:12–21.

36. Amaral EC, Moreno-Uribe AM, Bracarense AQ. Effects of PTFE on operational characteristics and diffusible H and O

contents of weld metal in underwater wet welding. J Manuf Process. 2021;61:270–9. https://doi.org/10.1016/j.jmapro.2020.11.018.

37. Moreno-Uribe AM, Bracarense AQ, Pessoa EC. The effect of polarity and hydrostatic pressure on operational characteristics of rutile electrode in underwater welding. Materials. 2020;13(21):5001. https://doi.org/10.3390/ma13215001.

38. Moreno-Uribe AM, Romanelli SCGA, Ribeiro MPH, Bracarense QA. Estudio de la corriente de transición en GMAW (MIG/MAG). Ingeniare Revista chilena de ingeniería. 2020;28(3):528–39. https://doi.org/10.4067/S0718-330520200000300528.Spanish.

39. Klett J, Hassel T. Influence of stick electrode coating's moisture content on the diffusible hydrogen in underwater wet shielded metal arc welding. Adv Mater Sci. 2020;20(4):27–37. https://doi.org/10.2478/adms-2020-0020.

40. Klett J, Wolf T, Maier HJ, Hassel T. The applicability of the standard DIN EN ISO 3690 for the analysis of diffusible hydrogen content in underwater wet welding. Materials. 2020;13:3750. https://doi.org/10.3390/ma13173750.

41. Castellanos OM, Moreno-Uribe AM, Ramón-Ramón SA, Jácome JL. Evaluación de la transferencia metálica y estabilidad del proceso gmaw. Revista UIS ingenierías. 2021;20(3):47–60. https://doi.org/10.18273/revuin.v20n3-2021003. (**Spanish**).

42. Dutra CJ. Ciência e tecnologia da soldagem a arco voltaico: dos fundamentos às modernas técnicas. Florianópolis: Editora Alfa Centauri. Portuguese; 2023.

43. Guo N, Cheng Q, Fu Y, Du Y, Zhang X, Feng J. Investigation on the mass transfer control, process stability and welding quality during underwater pulse current FCAW for Q235. J Manuf Process. 2019;46:317–27. https://doi.org/10.1016/j.jmapro.2019.08.022.

44. Silva DCC, Scotti A. Using either mean or RMS values to represent current in modeling of arc welding bead geometries. J Mater Process Technol. 2017;240:382–7. https://doi.org/10.1016/j.jmatprotec.2016.10.008.

45. Xu X, Liu S, Bang KS. Comparison of metal transfer behavior in electrodes for shielded metal arc welding. Int J Korea Weld Soc. 2004;4(1):15–22.

46. Ghasemi Y, Emborg M, Cwirzen A. Estimation of specific surface area of particles based on size distribution curve. Mag Concr Res. 2018;70(10):533–40. https://doi.org/10.1680/jmacr.17.00045.

47. Guo N, Zhang X, Fu Y, Luo W, Chen H, He JL. A novel strategy to prevent hydrogen charging via spontaneously molten-slag-covering droplet transfer mode in underwater wet FCAW. Mater Design. 2023. https://doi.org/10.1016/j.matdes.2023.111636.

48. Santos VR. Influências do oxigênio do gás de proteção em propriedades do metal de solda na soldagem hiperbárica MIG/MAG até 111 bar. Doctoral thesis. Federal University of Rio de Janeiro. Portuguese. 2001.

49. Fischer WA, Schumacher JF. Die Sättigungslöslichkeit von Reineisen an Sauerstoff vom Schmelzpunkt bis 2046 °C, ermittelt mit dem Schwebeschmelzverfahren. Archiv für das Eisenhüttenwesen. 1978;49(9):431–5 (**German**).

50. Hazlett TH. Coating ingredients influence on surface tension, arc stability and bead shape. Weld J. 1957;36(1):1.

51. Pope AM. Oxygen and hydrogen control in shielded metal underwater wet welding. Doctoral thesis. Colorado School of Mines. 1995.

52. Chen JH, Kang L. Investigation of the kinetic process of metal-oxygen reaction during shielded metal arc welding. Weld J. 1989;68(6):245–51.

53. Corderoy DJH, Wills B, Wallwork GR. Gas/weld metal reactions in MIG arc plasma. In: weld pool chemistry and metallurgy international conference; 1980. p. 147–53.

54. Tomić T, Kožuh Z, Garašić I, Samardžić I. Effects of hydrogen upon the properties of thermo mechanical controlled process (TMCP) steel. Metalurgija. 2016;55(1):99–102.

55. Engel L, Klingele H. Rastermikroskopische Untersuchungen von Metallschaden. German: Verlag Hanser; 1982.

56. Bøjesen ED, Iversen BB. The chemistry of nucleation. CrystEngComm. 2016;18(43):8332–53. https://doi.org/10.1039/C6CE01489E.

57. Castellanos-Gonzalez OM, Rodríguez-Arias A, Moreno-Uribe AM, Jácome-Carrascal JL. Particularidades de la transferencia metálica y la aplicación de corriente pulsada en soldadura submarina. Revista UIS Ingenierías. 2022;21(4):1–14. https://doi.org/10.18273/revuin.v21n4-2022001. (**Spanish**).

58. Krivtsun I, Maksimov S, Kvasnytskyi V. Welding and cutting under water. Weld Metallic Mater. 2023. https://doi.org/10.1016/B978-0-323-90552-7.00013-4. (**Elsevier**).